Available online at www.sciencedirect.com
ScienceDirect
International Journal of Solids and Structures 44 (2007) 1900–1926
INTERNATIONAL JOURNAL OF SOLIDS and STRUCTURES
www.elsevier.com/locate/ijsolstr

Shear band propagation from a crack tip subjected to Mode II shear wave loading

Z. Zhang, R.J. Clifton *

Division of Engineering, Brown University Providence, RI 02912, USA

Received 9 May 2006; received in revised form 26 September 2006
Available online 30 September 2006

Abstract

Results are reported for pressure–shear plate impact experiments in which pre-cracked 4340 steel plates are subjected to Mode II loading. Experiments show the propagation of a shear band ahead of the initial crack. Finite element simulations are used to interpret the results. Normal and transverse velocity–time profiles measured at the rear surface of the target can be simulated reasonably well using even an elastic model for the material response. A propagating shear band is obtained when the material is modeled as having reduced shearing resistance described by a thermo-viscoplastic power law, and complete loss of shearing resistance when the shear strain reaches a critical value. However, the predicted speed of propagation of the tip of the shear band is substantially less than required to explain the lengths of the bands observed in the experiments. Adjustments of parameters of the power-law model have little effect on the overall length of the band. Possible reasons for differences between predicted and measured shear band speeds are examined. Further reduction in the shearing resistance in the shear band appears to be essential for the simulated bands to be as long as those observed in the experiments.
© 2006 Elsevier Ltd. All rights reserved.

Keywords: Dynamic fracture; Crack tip plasticity; Metallic materials; Stress waves; Plate impact; Shear band

1. Introduction

The objective of the present study is to understand the shearing response of cracks in 4340 VAR steel under intense Mode II dynamic loading. Although, under impact loading, cracks are often subjected to shear loading, shear failure is much less thoroughly studied than tensile failure. This difference is due partly to the lack of experimental configurations for shear loading and partly to the lack of appropriate physical models describing the less well known failure mechanisms in shear. Understanding the competition between shear band formation and shear crack propagation is important for the explanation of shear failure and is an important part of the current investigation.

* Corresponding author. Tel.: +1 401 863 2855; fax: +1 401 863 3095.
E-mail address: clifton@engin.brown.edu (R.J. Clifton).

0020-7683/$ - see front matter © 2006 Elsevier Ltd. All rights reserved.
doi:10.1016/j.ijsolstr.2006.09.030

Experimental configurations for studying high speed shear crack problems are limited. The most commonly used method involves torsional Kolsky bar (split Hopkinson bar). Such work can be found in Follansbee (1985), Hartley et al. (1985), Field et al. (1994), Mgbokwere (1996), and Ramesh and Narasimhan (1996), as well as many others. Another configuration, first proposed by Kalthoff (2000), involves impact on the edge of a double-notched plate. A shadow optical observation method is used to monitor the Mode II crack tip loading. Kalthoff (1987) used his configuration to study the shear failure of epoxy resin, steel (X2 NiCoMo1895), and an aluminum alloy(Al 7075). A variation of the Kalthoff configuration involves a single-notched plate used by Mason et al. (1994), Zhou et al. (1996b) and Guduru et al. (2001). Mason et al. (1994) used the method of coherent gradient sensing(CGS) to study deformation fields around pre-notched C-300 steel plates loaded dynamically in Mode II. The single-notched plate configuration was also used by Zhou et al. (1996b) on both C-300 steel and a titanium alloy while Lambros and Rosakis (1994) used the CGS method on cracks in PMMA/4340 steel and PMMA/aluminum bimaterial specimens. Guduru et al. (2001) employed 2D high speed infrared camera to provide thermal images for shear band initiation and propagation in C-300 steel. Corresponding computational results were provided by Liu et al. (1995) for the Lambros and Rosakis (1994) experiments, by Zhou et al. (1996b) for the Zhou et al. (1996a) experiments, and Li et al. (2001) for the Guduru et al. (2001) experiments.

A principal conclusion of the Kalthoff, and Kalthoff-like, experiments is that at sufficiently high impact velocities a shear band is propagated ahead of the notch and its pre-crack extension. Furthermore, in the latter experiments (Zhou et al. (1996a) and Guduru et al. (2001)) simultaneous temperature measurements show substantial temperature increases in the vicinity of the band. In order to simulate the long bands that are generated, the computational models (Zhou et al. (1996b)) take the material within the band to be a fluid. No mechanism is offered to explain how a high-strength steel loses so much of its initial shearing strength that it can be characterized as a viscous fluid – before the work input is adequate to raise the temperature to a substantial fraction of the melting temperature.

A plate impact configuration, involving impact of parallel plates, is used in the current investigation. This configuration is similar to the one developed by Ravichandran and Clifton (1989) to study Mode I fracture. However, the current configuration involves pressure–shear impact instead of normal impact, in order to impose shear loading. An advantage of this approach is the simplicity of the loading since the loading waves incident on the crack are plane waves. A disadvantage is that the stress and deformation at the crack plane cannot be determined directly but must be related to velocity–time profiles measured at the rear surface of the target plate. For the pressure–shear impact configuration, all three fracture modes can be investigated. Experimental results for the Mode III configuration were reported in Zhang and Clifton (2003). The pressure–shear impact configuration is shown in Fig. 1. The initial half-plane crack is grown under fatigue loading in order to obtain a crack with a sharp tip. The crack is subjected to a compressive pulse, a shear pulse, and a reflected tensile pulse during the time of interest. After the compressive pulse passes the crack plane, the

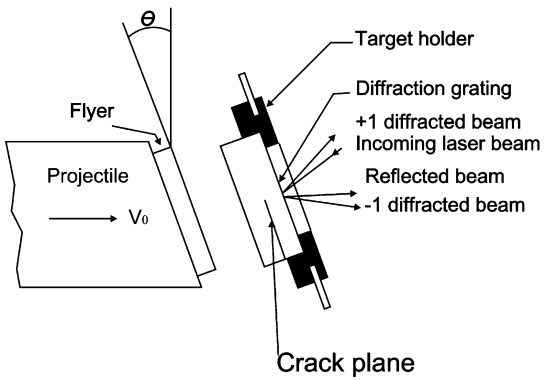

Fig. 1. Schematic of pressure–shear plate impact configuration for subjecting a part-through crack in a target plate to shear wave loading. The diffraction grating on the rear surface enables the monitoring of both normal and transverse motion by means of laser interferometry. The target orientation shown is for a Mode II loading.

incident shear wave arrives to subject the unloaded crack to shear wave loading. This loading ends before the reflected tensile pulse reaches the crack plane. Both transverse and normal components of the target motion are monitored at one pre-determined position on its rear surface by means of a transverse displacement interferometer (TDI, see Kim et al., 1977) and a normal displacement interferometer (NDI).

Experimental results are compared with results from numerical simulations. Both normal and transverse velocity–time profiles are found to agree reasonably well with those obtained from numerical simulations. Plasticity has a relatively small effect on the velocity–time profiles. Also, through numerical simulations, certain recording and interpretation difficulties are identified to be associated only with the Mode II loading. The approach of using short focal length lenses, which is sufficient for Mode III experiments, is insufficient for Mode II experiments. A new optical approach using a combined lens-beamsplitter in a TDI with imaging optics is used to minimize the effects of surface rotation in Mode II experiments. Satisfactory results are obtained.

After each experiment, the target is recovered and examined using various microscopies. Long shear bands are found in front of Mode II loaded cracks. In order to simulate the formation and propagation of the shear band, mesh sizes as small as 1.25 μm are used. A mesh size of 5 μm is used for most simulations. Mesh size effects are also investigated. It is found that the smaller the mesh, the higher the final temperature and narrower the band. Based on a quadratic dependence of error on mesh size, a nominal zero-size temperature distribution is found by extrapolation. These temperatures are still smaller and more limited in extent than expected from the microscopic observations.

Introduction of a shear–strain failure model results in a well-defined band-like feature. The final temperature of the band is, however, lower than obtained for models that do not allow for shear–strain failure. On the other hand, the length of the band is significantly greater. Changes in parameters in a power-law plasticity model had very little effect on the final temperature distributions. These results suggest that a more catastrophic failure process may need to be considered.

2. Experimental velocity–time profiles

The experimental configuration for pressure–shear plate impact studies of dynamic failure of a 4340 VAR steel (200 °C temper, $R_c = 52$) is shown in Fig. 1. The target is a disk containing a pre-fatigued, mid-plane crack that has propagated halfway across the diameter of the specimen. The target is impacted by a flyer plate mounted on a projectile tube and traveling at a velocity V_0. The flyer plate and the target are parallel but inclined at an angle θ relative to their direction of approach. The dimensions of the target and flyer are designed such that the shear wave generated at the impact face arrives at the crack plane after the normal wave generated at the impact face passes through. Then, during the duration of the shear pulse, there is only shear wave loading at the crack plane. Details of the experimental procedures used for the experiments reported are given in Zhang (2005).

Table 1 shows a summary of the various shots reported here. The 'S.D.' stands for "shearing direction" where a '+' sign indicates shearing of the impact face toward the open fatigue crack and '−' sign indicates shearing in the opposite direction. The distance a is the estimated distance from the position at which the motion is monitored to the projection of the crack tip onto the rear surface of the target. The stress σ_m is the Mises stress $\sigma_m \equiv \sqrt{J_2}$ where J_2 is the second invariant of the stress deviator tensor. Fig. 2 shows all four oscilloscope traces for Shot 0002. The top two are NDI traces and the bottom two are TDI traces. A short focal-length-lens setup is used. Three lenses used for each of the three incident and diffracted beams have relatively short (when compared with regular setups) focal lengths ($f = 105$ mm for the NDI traces and

Table 1
Summary for various plate impact shots

Shot	H_0 (mm)	H_1 (mm)	H_2 (mm)	V_0 (mm)	Mode	S.D. (+/−)	Tilt (mrad)	a (mm)	σ_m (MPa)
0001	2.14	5.35	5.65	124	II	–	0.9	3.8	1730
0002	2.25	5.80	5.27	127	II	+	1.0	0.4	1773
0103	2.34	5.14	5.16	91	II	+	0.4	3.0	1270

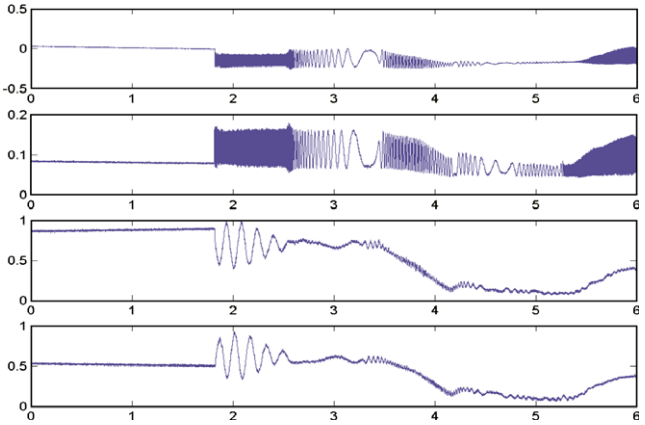

Fig. 2. All traces of Shot 0002.

$f = 85$ mm for the TDI traces) to reduce the shift of the beams due to rotation of the rear surface that occurs when diffracted longitudinal waves arrive. The same setup has been used successfully in Mode III experiments: Zhang and Clifton (2003). In the Mode II experiment, Fig. 2, the effect of the rotation of the rear surface is substantially greater and the TDI trace is reduced to small oscillations about a mean intensity that is decreasing to near zero over a time of approximately 0.5 μs. Through careful post-processing the TDI traces can be reduced to obtain the transverse velocity. However, the resolution of the transverse motion is not as good as for the Mode III traces. There are parts of the TDI signal where the oscillations are so weak that the transverse motion cannot be determined. Fig. 3 shows the corresponding time–distance diagram for Shot 0002. Longitudinal wave fronts are shown as solid lines and shear waves fronts are shown as dashed lines. The Mode II experiments are inherently more difficult to interpret than the Mode III experiments because diffraction of the plane shear wave by the semi-infinite crack results in the generation of a diffracted dilatational wave as well as a diffracted shear wave. Furthermore, when this diffracted dilatational wave arrives at the monitoring position on the rear surface, ahead of the initial crack tip, the associated component of lateral motion is in a direction perpendicular to the lines of the diffraction grating. Consequently, the lateral motion due to the diffracted dilatational wave is superimposed on the transverse motion of the plane shear wave, which is the primary wave that the TDI is intended to monitor. Moreover, the amplitude of the lateral motion is significant relative to the

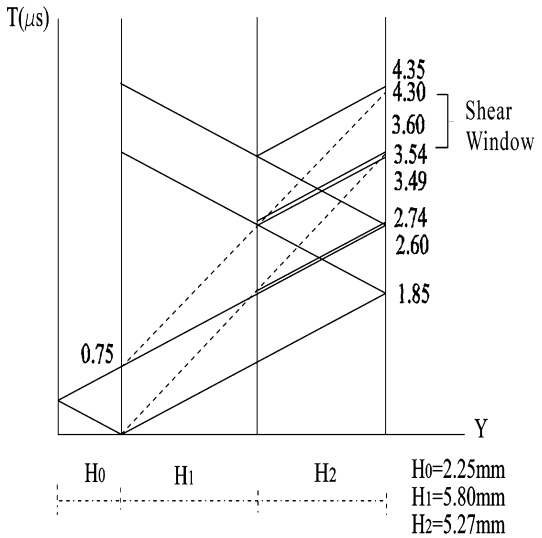

Fig. 3. Time–distance diagram for Shot 0002.

amplitude of the plane shear wave. Furthermore, the normal velocity associated with the diffracted dilatational wave varies strongly with the angle from the normal to the crack plane to the radius vector locating a point along the rear surface, ahead of the crack tip. As a result the rotation of the rear surface is substantial and this rotation results in the loss of intensity shown in Fig. 2. The combined effects of the rotation of the rear surface due to the cylindrical dilatational wave resulting from the diffraction of the plane shear wave by the semi-infinite crack and the cylindrical dilatational wave resulting from the diffraction of the reflected, plane longitudinal wave by the semi-infinite crack are additive and can result in surface rotations as large as 13 mrad at monitoring positions that are approximately 1.0 mm in front of the crack tip.

Figs. 4 and 5 show the normal and transverse velocity–time profiles of the rear surface motion for a Mode II experiment, Shot 0001, at an impact velocity of 124 m/s. The normal velocity–time profile looks similar to that obtained for Mode III experiments while the transverse profile is quite different. When the compressive pulse reaches the rear surface at 1.82 μs, the normal velocity jumps to 104 m/s and then gradually approaches 117.8 m/s, which is the corresponding normal component of the projectile velocity. After the initial compressive pulse passes through at approximately 2.6 μs, the normal velocity of the rear surface drops quickly to 16 m/s. It then decreases gradually to essentially zero. This tail on the compressive pulse is attributed primarily to a small amount of plastic deformation that occurs at these impact velocities. It should be noted however, (see Fig. 3) that the diffracted dilatational wave generated by the incident shear wave arrives at approximately the same time as the unloading longitudinal wave. Thus, the tail of the compressive pulse is associated with at least two physical effects so a complete numerical simulation is required to interpret the observations.

When the reflected tensile pulse arrives at the crack plane it generates two cylindrical diffracted waves: a dilatational wave and a shear wave (as well as a head wave). From Fig. 4 the front of the dilatational wave arrives at the monitoring point on the rear surface of the target at 3.42 μs. The normal velocity of the rear surface increases gradually to a velocity of 16 m/s at 3.62 μs, remains approximately constant until 3.86 μs, and then decreases gradually to approximately 10 m/s. At 4.19 μs the normal velocity drops quickly, changes sign, and takes on negative values – reaching a minimum value of approximately −7 m/s. As with the tail of the compressive pulse, the interpretation of this second pulse is also complicated by the arrival of more than one pulse during this time. From Fig. 4 one can see that the dilatational wave generated by the diffraction of the reflected tensile pulse from the crack plane arrives at the rear surface at approximately the same time as the cylindrical dilatational wave generated by the diffraction of the unloading shear wave. Again, a complete numerical solution is required to interpret these combined effects.

In Fig. 5, the initial tilt causes the transverse motion of the rear surface to show a small bump of approximately 6 m/s. The main shear pulse arrives at the rear surface at 3.30 μs. The transverse velocity drops to −16 m/s, decreases gradually to −69 m/s at 4.03 μs, and then increases to near zero at approximately 4.2 μs. It is interesting to note that the minimum value of −69 m/s is significant lower than the corresponding transverse component of the projectile velocity, i.e., −38 m/s. This behavior is quite different from that of the

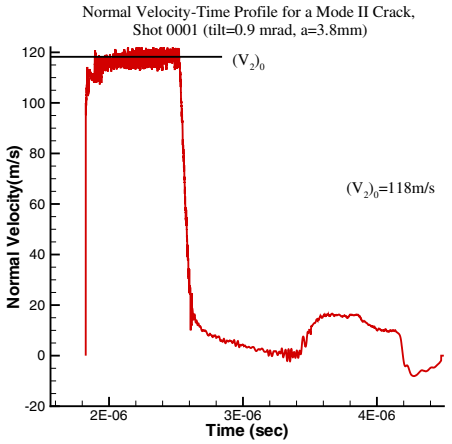

Fig. 4. Normal velocity–time profile for Shot 0001, $V_0 = 124$ m/s, $\theta = 18°$.

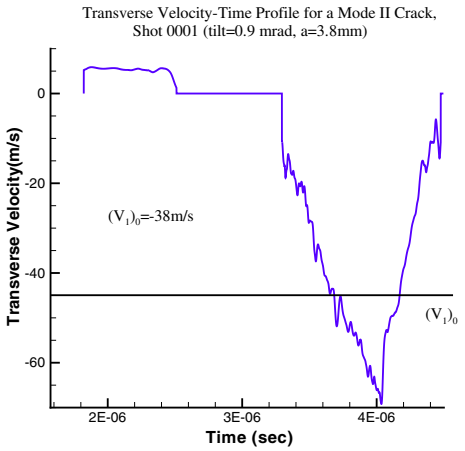

Fig. 5. Transverse velocity–time profile for Shot 0001, $V_0 = 124$ m/s, $\theta = 18°$.

Mode III experiments where the maximum amplitude value of the transverse velocity is always smaller than the transverse component of the projectile velocity. However, these differences can easily be reconciled by noting that (see Fig. 3) during the refraction of the main shear pulse from the rear surface the transverse motion at the monitoring point is affected by the diffracted dilatational waves generated by both the plane tensile pulse and the unloading plane shear wave. The latter pulse is quite strong (the strength of the longitudinal wave is several times that of the shear wave) and is inclined to the normal of the rear surface. As a result, this pulse causes substantial transverse motion at a monitoring position ahead of the crack tip. For the Mode II case this transverse motion is in the direction recorded by the TDI so it has a major effect on the recorded transverse velocity. In contrast, for the Mode III case the transverse motion induced by the reflected dilatational wave is perpendicular to the direction of the motion recorded by the TDI so there is no effect of the reflected dilatational wave on the transverse motion recorded at the rear surface. Moreover, for Mode III, there is no diffracted dilatational wave caused by the plane shear waves so that in the Mode III case the TDI record describes solely the motion due to the plane shear pulse and the diffracted shear pulse.

Figs. 6 and 7 show the normal and transverse velocity profile of another Mode II experiment at a similar impact velocity. The general features of the response are similar to those of Shot 0001. Because the monitoring position is significantly closer to the crack tip ($a = 0.5$ mm) in this experiment, the diffracted tensile pulse has a larger magnitude: 46 m/s. The peak value of the transverse velocity during the main shear pulse is again larger

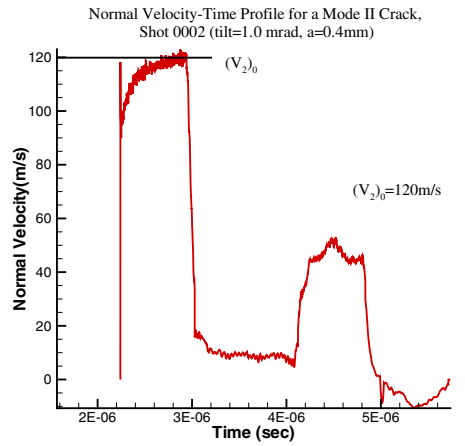

Fig. 6. Normal velocity–time profile for Shot 0002, $V_0 = 127$ m/s, $\theta = 18°$.

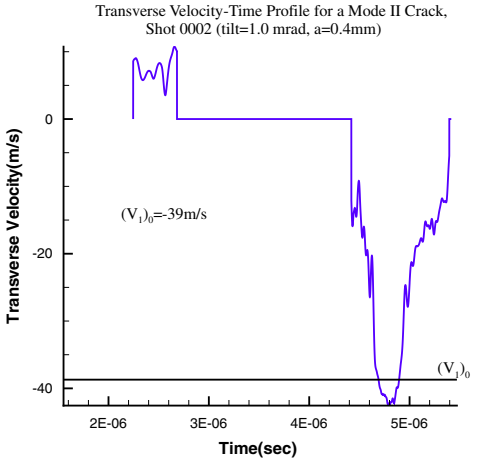

Fig. 7. Transverse velocity–time profile for Shot 0002, $V_0 = 127$ m/s, $\theta = 18°$.

than the transverse component of the projectile velocity, although the difference is smaller because of the normal to the diffracted dilatational wave being more nearly aligned with the normal to the rear surface. Again there is a reversal of sign in the normal velocity in the tail of the diffracted pulse.

Fig. 2 shows that the short focal length lenses works well for the NDI, but not for the TDI. There is a significant loss in intensity in the TDI signal after the shear pulse reaches the rear surface. As discussed previously, this loss in intensity is caused by the rotation of the rear surface due to the arrival of diffracted dilatational waves. Additional dimensional constraints are imposed by the requirement that the optical components fit within the vacuum (target) chamber where the impact occurs. The setup is shown in Fig. 8. For this setup, $F = 500$ mm, $f = 250$ mm, $b = 12.7$ mm, $a = 0.56$ mm, $f' = 75$ mm and $d = 19$ mm. Details of this setup can be found in Zhang (2005). Note that, in order to prevent damage to the NDI lens (i.e., the lens with focal length F), this lens has been positioned outside of the vacuum chamber. The combined beamsplitter and lens is placed inside the chamber, away from the path of the projectile and to the right of the target holder, and can be used for multiple tests. All other components are located inside the chamber, in the path of the projectile, and are destroyed in each test (Fig. 9).

All four traces for a shot (Shot 0103) using the revised optical layout are shown in Fig. 10. The revised layout works well. The TDI signals are strong throughout the duration of the main shear pulse. The NDI signal

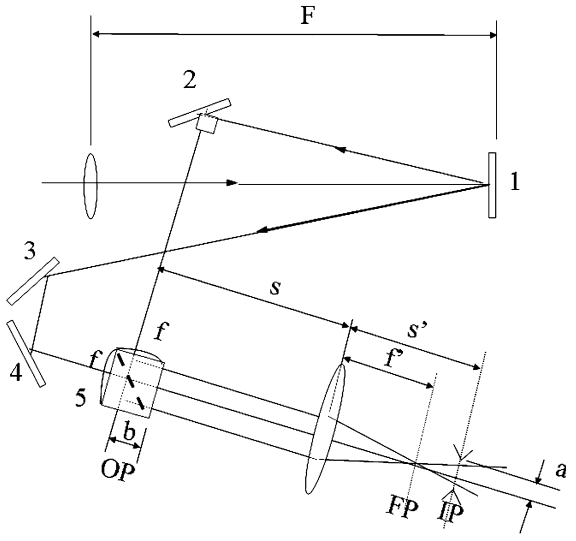

Fig. 8. Optical layout for short- focal-length, imaging TDI.

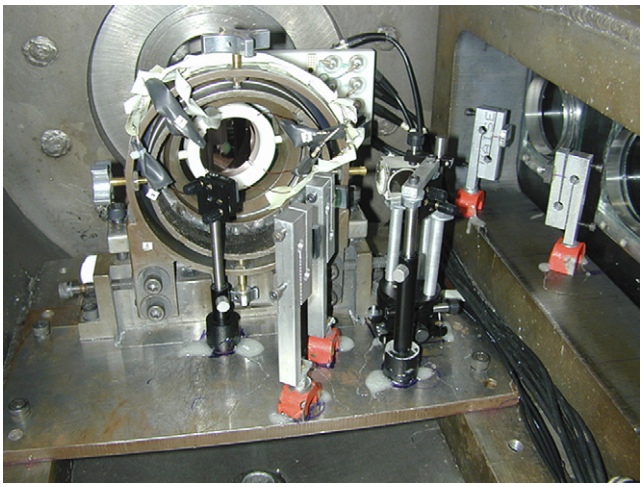

Fig. 9. The target chamber, viewed from the rear.-

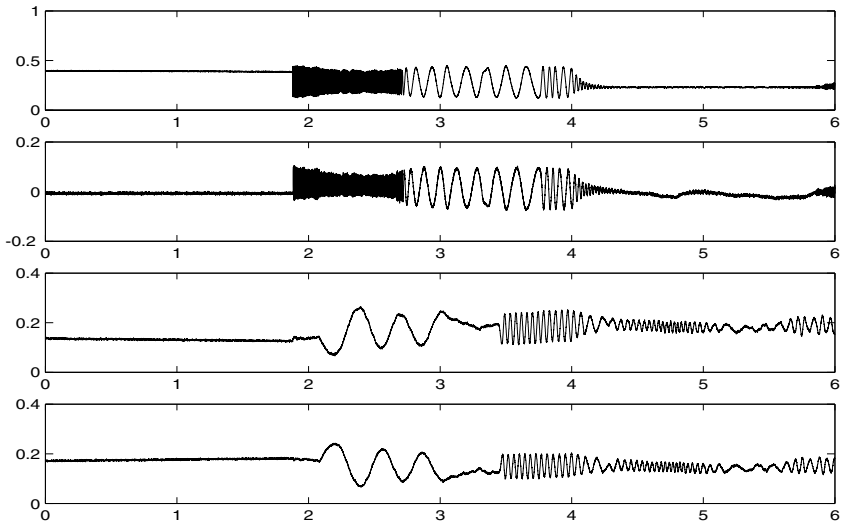

Fig. 10. All traces for Shot 0103.

starts strong, but becomes attenuated as the normal displacement increases. By the end of the shear pulse, the magnitude of the NDI signals is of the strength of the background noise. However, its higher frequency make it easier to extract the corresponding motion than for the TDI. Overall, the revised layout appears to have provided a reasonable compromise to the design problem of meeting the physical constraints and keeping the costs down.

Figs. 11 and 12 show the corresponding normal and transverse components of the velocity history at the rear surface. As shown in Fig. 11, the normal velocity rises quickly to that of the normal component of the projectile velocity. Unlike its higher velocity counterpart, there is no curved portion. The normal velocity stays at that level for the duration of the incident pulse. Then it falls quickly to approximately 2.0 m/s. Again, unlike its higher-velocity counterpart, there is no visible plastic tail. Beginning at the arrival of the longitudinal wave diffracted from the crack, at approximately 3.69 μs, a second positive pulse arrives and continues until approximately 4.40 μs. After that the normal velocity falls, becomes negative, and remains at approximately −10.8 m/s for the remainder of the time of interest.

As for the transverse velocity profile shown in Fig. 12, the initial tilt-induced pulse is small, approximately 2 m/s, as expected for the small tilt angle of approximately 0.4 mrad. The transverse velocity then vanishes

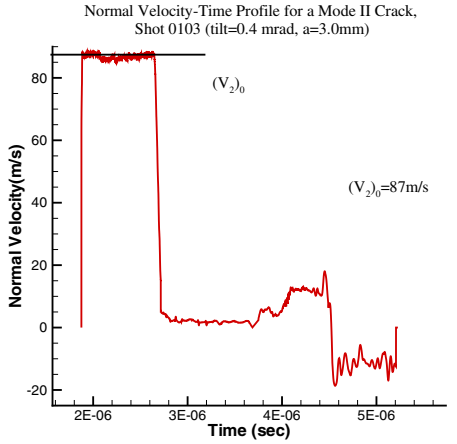

Fig. 11. Normal velocity–time profile for Shot 0103, $V_0 = 91$ m/s, $\theta = 18°$.

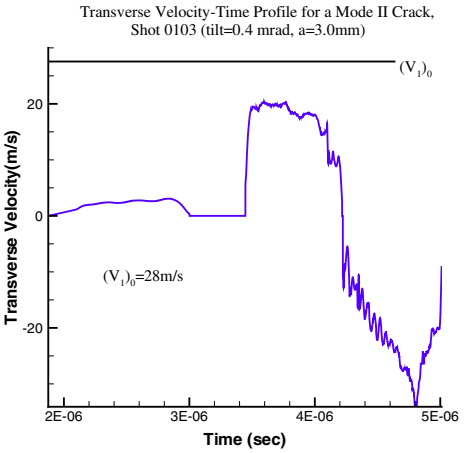

Fig. 12. Transverse velocity–time profile for Shot 0103, $V_0 = 91$ m/s, $\theta = 18°$.

until the main transverse pulse reaches the rear surface at 3.43 μs. The transverse velocity then rises sharply to 19.8 m/s and stays there until 3.76 μs. It then takes a small dip to 17.6 m/s and stays there until 4.01 μs. After that it quickly becomes negative when the longitudinal wave diffracted from the crack arrives. By 4.80 μs, the transverse velocity is −33.6 m/s. Further understanding of these wave profiles will emerge as the numerical simulations in Section 3 are considered.

3. Numerical simulations of velocity–time profiles

Uniform meshes of 2D, 4-node, reduced-integration, plane strain elements are used for the Mode II crack problems. In the model geometry, shown in Fig. 13, both target and flyer plates are meshed. The thickness of the flyer is H_0, the distance from the front face of the target to the crack is H_1, and the distance from the crack

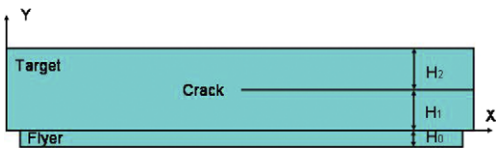

Fig. 13. Sketch of the model used in Mode II simulation.

to the rear face of the target is H_2. The two plates impact at $Y = 0$. The flyer occupies the region $-H_0 \leqslant Y \leqslant 0$ and the target occupies the region $0 \leqslant Y \leqslant H_1 + H_2$. Actual dimensions from the experiments are used with the exception that the circular geometry is replaced by strips with widths D_1 and D_2 corresponding to the diameters of the flyer and the target plates, respectively. With the 2D problem being simulated, various effects, such as tilt, surface roughness, friction, and etc. can be explored (see Zhang, 2005). The origin of the Cartesian system is located at the lower left corner of the target. Each element is a square with sides of length Δx. The initial conditions are

$$V_i = 0 \quad \text{for } 0 \leqslant Y \leqslant H_1 + H_2 \tag{1}$$

$$V_1 = V_0 \sin\theta \quad \text{and} \quad V_2 = V_0 \cos\theta \quad \text{for} \quad -H_0 \leqslant Y \leqslant 0 \tag{2}$$

The non-contacting faces of the plates are taken to be traction-free while the contacting surfaces are taken to satisfy either a no-slip condition or a Coulomb friction condition. The material is taken to be elastic initially. No crack advance is considered. The initial velocity V_0 is taken to be 125 m/s and the angle θ is taken to be 18°. For these values, the normal and transverse components of the projectile velocity are $V_2 = 118.8$ m/s and $V_1 = 38.6$ m/s. The diameter of the target is $D_t = 62.4$ mm, the front thickness is $H_1 = 5.4$ mm and the back thickness is $H_2 = 5.6$ mm. The diameter of the flyer is $D_f = 59$ mm and the thickness of the flyer is $H_0 = 2.2$ mm. The mass density is $\rho = 7600$ kg/m^3, the Young's modulus is $E = 208$ GPa and the Poisson's ratio is $v = 0.3$. The corresponding longitudinal wave speed is $c_1 = 5983$ m/s, the transverse wave speed is $c_2 = 3124$ m/s and the Rayleigh wave speed is $c_R = 2987$ m/s.

The wave fronts for Mode II cases are shown in Fig. 14. At the instant shown, the compressive pulse has passed through the crack plane and the shear wave has begun to diffract from the crack. Because of the coupling in the diffraction of waves by the crack, shearing towards the crack tip is different from shearing away from the crack tip. Figs. 15 and 16 show the difference in various normal and transverse velocity profiles. Three cases are compared, namely shearing in positive X direction (i.e., '+' symbol in S.D. column of Table 1), no shearing at all, and shearing in the negative X direction. The comparisons are made for the position $a = 0$. As shown in Fig. 15, the initial compressive pulse remains the same for all cases. After the compressive pulse has reflected from the rear surface, the normal motion caused by the diffracted longitudinal wave, generated by the plane shear wave incident on the crack plane, arrives at the rear surface. Shearing in the opposite directions leads to opposite normal motions. Similarly, the shear-wave-induced contribution to the diffracted tensile pulse (i.e., the second pulse in Fig. 15) is of opposite sign for shearing in opposite directions. As shown in Fig. 16, the transverse motion stays opposite for shearing in the opposite directions until the shear wave caused by the reflected tensile pulse arrives. After that, the transverse motion decreases monotonically. Early parts of the profiles show small numerical fluctuations that should not appear in the experimental records.

Lacking accurate measurement of the inclination of the crack plane, the magnitude of the reflected tensile wave may be a better choice to determine the monitoring position than that of the arrival time of that same wave. The effect on the velocity–time profiles of a crack plane not being parallel to the impact plane can be found in Zhang (2005). For comparison purposes the location 'a' of the monitoring position is taken to be the one that provides the best fit between measured and simulated velocity–time profiles. Figs. 17–22 show comparisons between the experimental data and the numerical calculations for normal and transverse

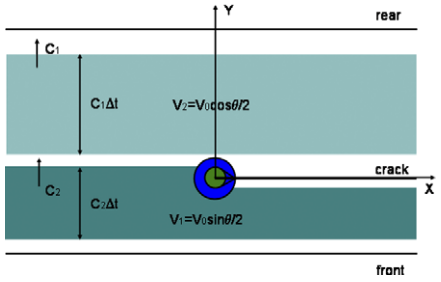

Fig. 14. Wave fronts for Mode II loading.

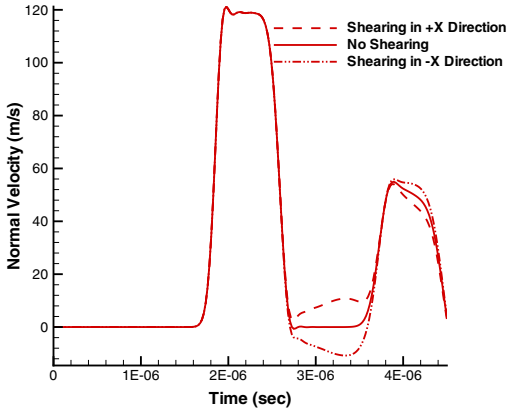

Fig. 15. Normal velocity–time profiles for different shearing directions.

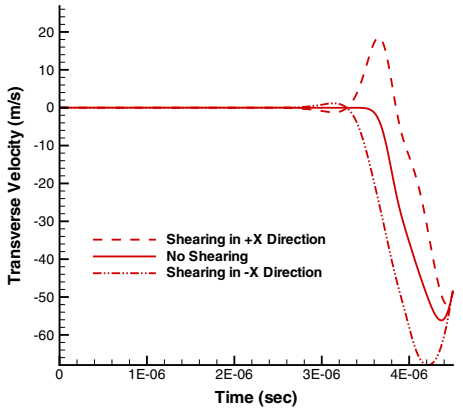

Fig. 16. Transverse velocity–time profiles for different shearing directions.

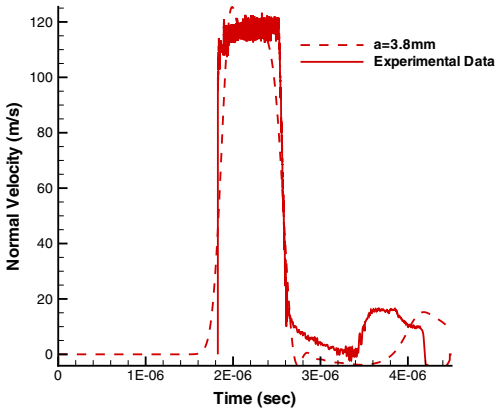

Fig. 17. Comparison of normal velocity–time profile for Shot 0001.

velocity–time profiles for Shots 0001, 0002, and 0103. The various a positions are estimated from the magnitude of the corresponding reflected tensile waves. As shown in Fig. 23, the quality in certain sections of the TDI signals for Shot 0002 are so bad that velocity information for those sections cannot be extracted. As a result, the main shear pulse is missed in Fig. 20.

Although the FEM calculations for an elastic material agree reasonably well with experimental records, the time at which the reflected tensile wave arrives does not agree fully. The shift in time is approximately 200 μs.

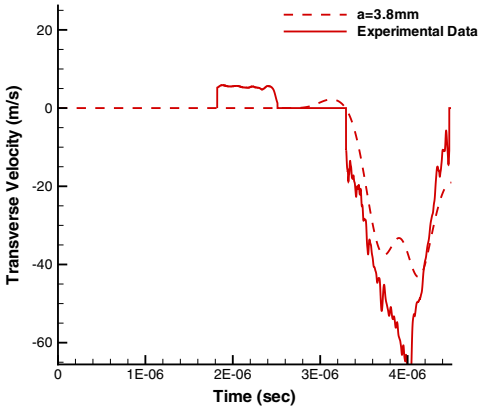

Fig. 18. Comparison of transverse velocity–time profile for Shot 0001.

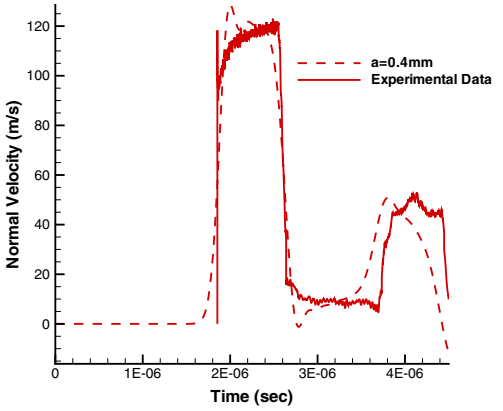

Fig. 19. Comparison of normal velocity–time profile for Shot 0002.

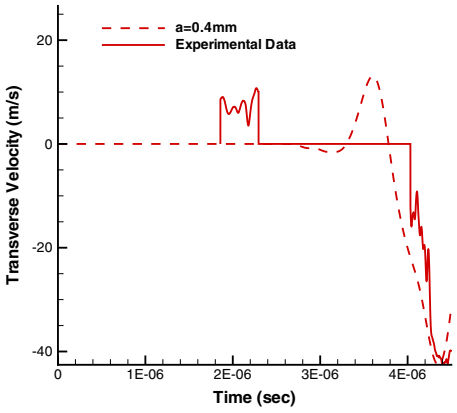

Fig. 20. Comparison of transverse velocity–time profile for Shot 0002.

One possible explanation is that the plane of the initial fatigue crack is not parallel to the impact face. Measurement of a post-experiment sample seems to confirm such an explanation. With the help of FEM calculations, it is possible to investigate the effect of an inclined initial crack. Fig. 24 shows the FEM model used. D_c is the deviation of the real crack tip position from its projected position. A positive D_c corresponds to deviation of the crack in the positive Y direction. Figs. 25 and 26 show the comparison of normal and

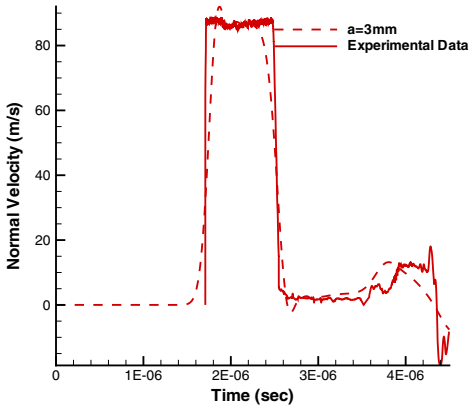

Fig. 21. Comparison of normal velocity–time profile for Shot 0103.

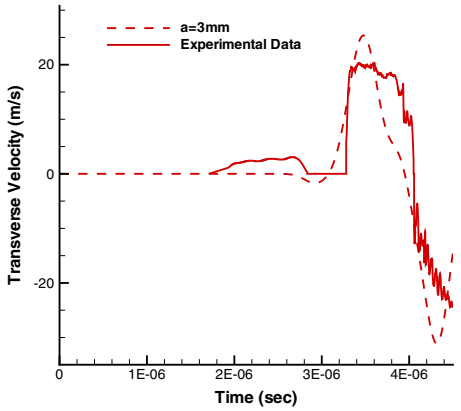

Fig. 22. Comparison of transverse velocity–time profile for Shot 0103.

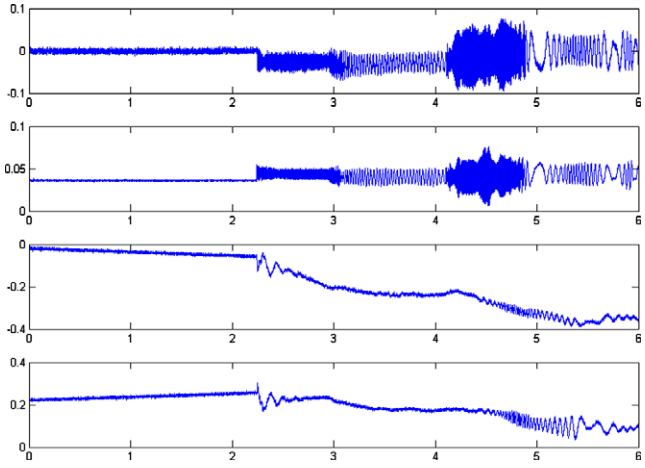

Fig. 23. All traces for Shot 0002.

transverse velocity–time profiles for various inclined crack planes. Rear surface velocity–time profiles are at $a = 0$. The main effects of an inclined crack plane are the shifts in velocity–time profiles caused by the reflected tensile wave. The time shifts are approximately 0.23 μs for the normal velocity–time profiles. This is the change

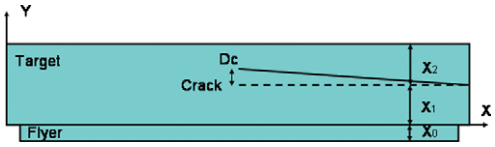

Fig. 24. The FEM Model for an inclined crack plane.

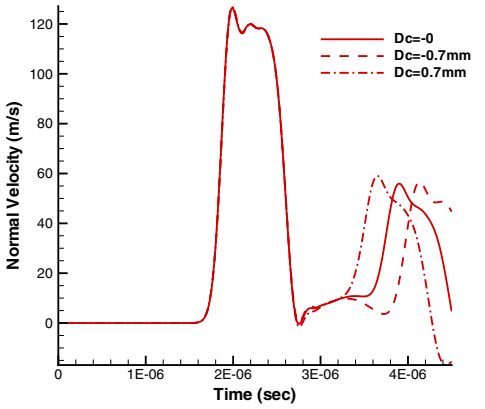

Fig. 25. Comparison of normal velocity–time profiles for various crack tip deviation at $a = 0$.

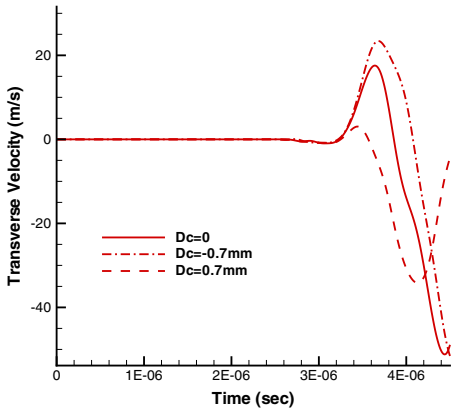

Fig. 26. Comparison of transverse velocity–time profiles for various crack tip deviation at $a = 0$.

in the round trip time for the normal wave for a crack-tip deviation of 0.7 mm. For the normal velocity–time profiles, there are no changes in the initial compressive pulse since the total target thickness remains the same. The magnitude of the normal velocity in the diffracted pulse increases a little for $D_c = 0.7$ mm. This increase in magnitude is due to the superposition of multiple waves. For the transverse velocity–time profiles, the time shift is approximately 200 ns and less uniform than its counterpart in the normal velocity–time profiles. This difference is due to the relatively larger change in the amplitude of the transverse velocity, especially for the case of $D_c = 0.7$ mm. Again the reflected tensile wave is the cause of this change in amplitude. Such a change can be troublesome if the amplitude is mis-identified. Overall, the exact position of the tip of the initial fatigue crack may need to be given more attention to match the experimental data more closely with computational results.

The effects of plasticity on velocity–time profiles are also explored. Three plasticity models, elastic-perfect plastic, exponentially strain hardening model, and a power law model, are considered with parameters fitted

from earlier experimental results, Tanimura and Duffy (1986), Clifton and Klopp (1985), and Zhang (2005). It is found that except for a very soft material, the velocity–time profiles obtained when plasticity is considered vary little from their elastic counterparts. Details can be found in Zhang (2005).

4. Microscopic observations

Fig. 27 shows a cross-sectional view of the recovered plate (Shot 0002), viewed in an optical microscope at a magnification of 200×. The direction of band propagation is from top to bottom. The left and right figures overlap by two photos. The surface has been etched in a 3% nital etchant. The band etches white in agreement with the usual observations of shear bands in steels (see, e.g., Rogers (1979)). The white-etched regions appear to be discontinuous near the tip of the band. These discontinuities probably are due to the restarting of the shear band upon the arrival of reflected waves.

Figs. 28 and 29 show SEM micrographs of the cross-section of the recovered plate for the same Mode II experiment, Shot 0002. Segments of the cross-section shown as (a)–(d) in Figs. 28 and 29 correspond to regions (a)–(d) identified in Fig. 27. The overall appearance of a shear band extending in front of the initial crack is quite similar to that reported in Zhang and Clifton (2003) for a Mode III experiment. The SEM micrographs show a long thin band with a length of 1.36 mm and a thickness of approximately 10 μm. Both the length and thickness of the band are comparable to those observed for the Mode III experiments at comparable impact velocities. The band appears to be quite uniform throughout its length. Again cracks run along the edges of

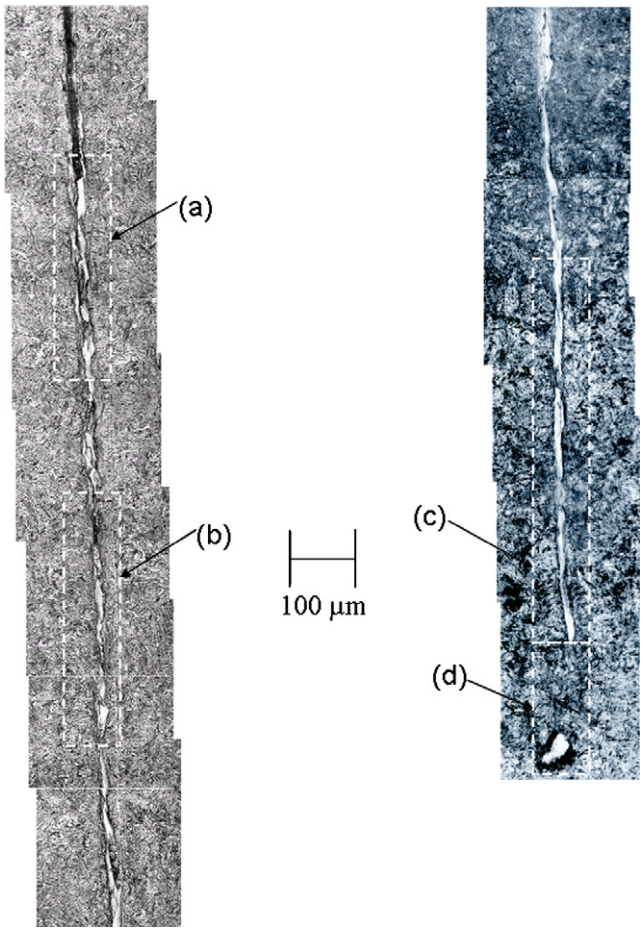

Fig. 27. Optical view of cross-section of final shear band for shot 0002.

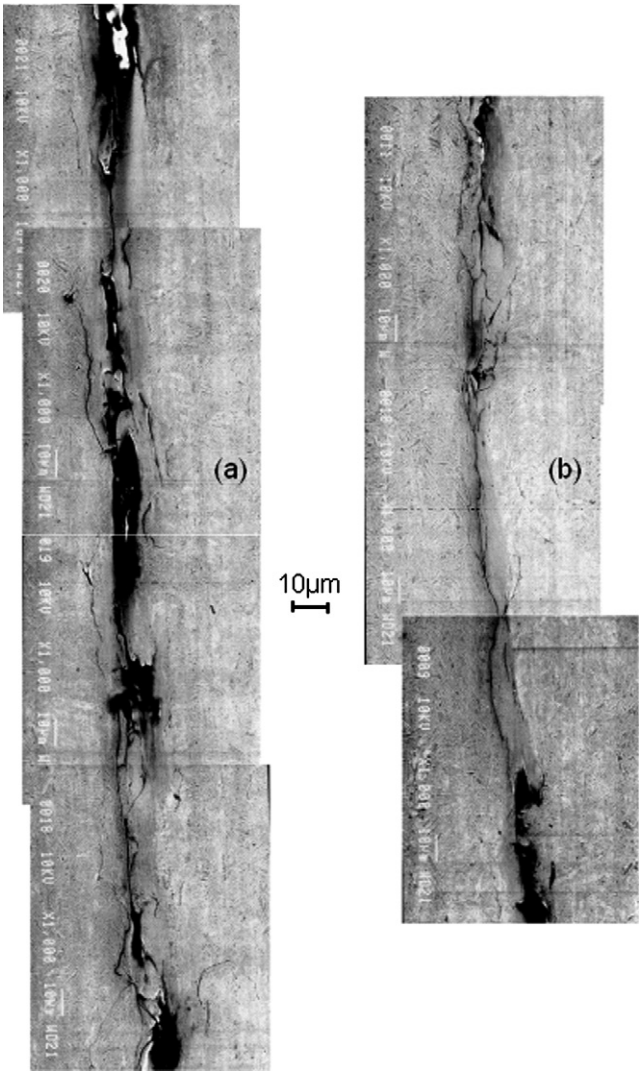

Fig. 28. SEM micrograph of cross-section of final shear band for Shot 0002 (segments (a) and (b)).

the band as well as within the band. As in the case of Mode III, the end of the band is characterized by a cracked region, a dark region where damaged material has been removed by the polishing process, and a crack bifurcation before the crack is finally arrested. These general features are observed in all of the Mode II experiments. To position the crack bifurcation region of the shear band relative to the optical micrograph shown in Fig. 27, identify the separated white region in Fig. 27 with the gray region in the bottom quarter of segment (d) of Fig. 29. Although difficult to see in Fig. 27, the crack bifurcation shown in Fig. 29 lies at the edge of the inclined white region.

5. Numerical simulation of shear band formation

Fig. 30 shows the sketch of the FEM model used for detailed simulations of the region in front of the crack tip. The geometry is limited by the requirement that before the end of the pulse arrives, no boundary wave affects the region in front of the crack tip. Thus, the dimensions H_1, H_2, L_1, and L_2 are constrained by:

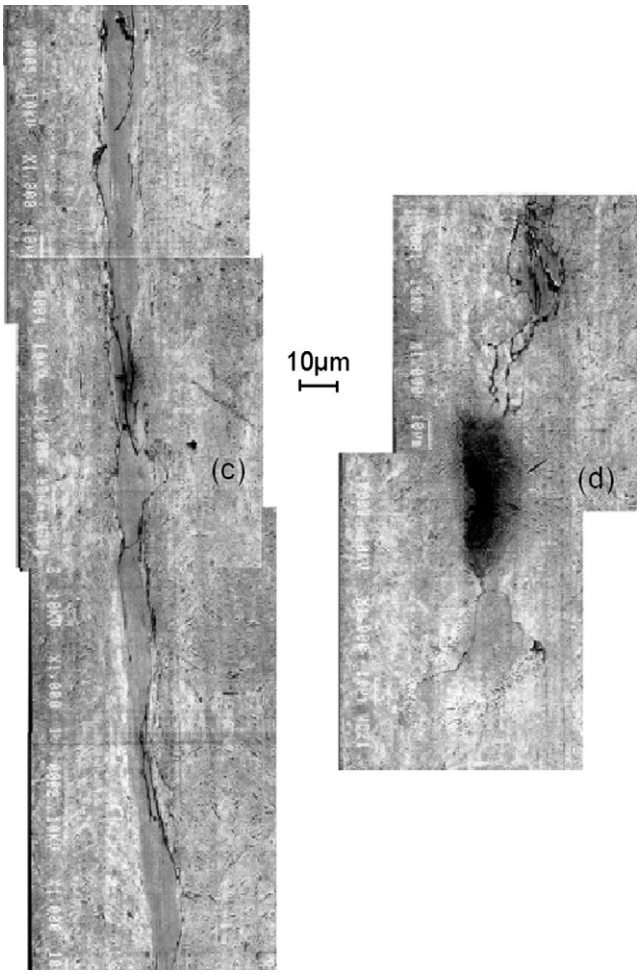

Fig. 29. SEM micrograph of cross-section of final shear band for Shot 0002 (segments (c) and (d)).

$$\begin{aligned}
&\frac{2H_2}{c_1} \geqslant \Delta t \\
&\frac{2H_1}{c_1} \geqslant \Delta t \\
&\frac{2L_2}{c_1} \geqslant \Delta t \\
&\frac{2L_1}{c_1} \geqslant \Delta t \\
&\frac{L - L_1 - L_2}{c_1} \geqslant \Delta t \\
&H_1 \geqslant c_2 \Delta t
\end{aligned} \tag{3}$$

where Δt is the duration of the incident shear pulse. It is convenient to have

$$\begin{aligned}
&H_1 = H_2 = L_1 = L_2 = \frac{c_1}{2}\Delta t \\
&L = 2c_1 \Delta t
\end{aligned} \tag{4}$$

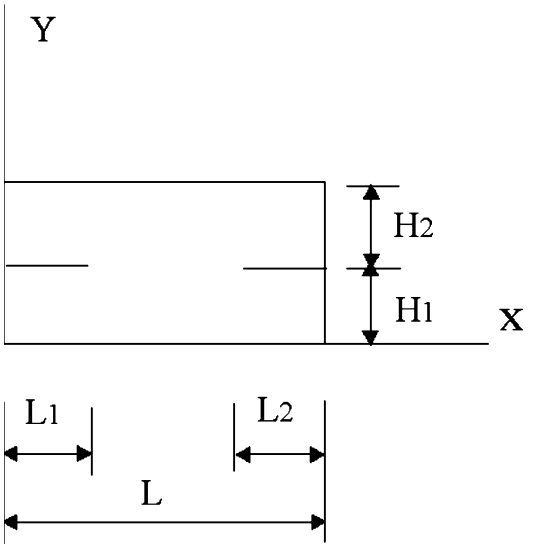

Fig. 30. Sketch of the model geometry for the 2D FEM simulations.

The thickness of the observed shear band generated in front of the existing crack tip is approximately 10 μm. In order to simulate its formation, the mesh size for the FEM calculations should be of that size, or preferably smaller. This requirement imposes significant demands on computational resources. Moreover, a license for ABAQUS Explicit must be available on whatever machine the calculation runs on. The IBM p690 supercomputer from NCSA at UIUC satisfies both requirements and was one of the most powerful machine available for academic users. It was used in our simulations. Only the response to the incident shear wave was simulated because the compressive pulse is essentially elastic and it passes through the crack plane before the shear pulse arrives. This simplification has no effect on the simulated waves generated by the arrival of the shear wave at the crack plane, while saving considerably on the computational effort by eliminating the need to consider the time between the arrival of the compressive pulse and the arrival of the shear pulse.

By using data contained in Tanimura and Duffy (1986) and Clifton and Klopp (1985) for various tempering conditions, a power law fit for the flow stress in shear can be found as:

$$\tau_{\mathrm{p}} = 1100\left(\frac{\gamma^{\mathrm{p}}}{0.005}\right)^{n}\left(\frac{\dot{\gamma}^{\mathrm{p}}}{400}\right)^{m}\left(\frac{\theta}{298}\right)^{l} \tag{5}$$

where $n = 0.03$, $m = 0.02$ and $l = -0.17$. This model for shearing resistance is used in the simulations of shear band formation.

Because temperature variation is important in the simulation of dynamic shear bands, coupled temperature–displacement elements are used. The thermal energy balance is given as:

$$\int_V \rho\dot{U}\,\mathrm{d}V = \int_S \mathbf{q}.\mathbf{n}\,\mathrm{d}S + \int_V \Gamma\,\mathrm{d}V \tag{6}$$

where V is the volume considered, S is its surface area, ρ is the mass density, $\dot{U}$ is the time rate of change of the internal energy, $\mathbf{q}.\mathbf{n}$ is the heat flux per unit area, and Γ is the heat supply per unit volume. The increase in internal energy with increasing temperature is defined as

$$\mathrm{d}U = C\,\mathrm{d}\theta \tag{7}$$

where C is the specific heat per unit mass, taken to be 477 J kg^{-1} K^{-1}. Heat conduction is assumed to follow the Fourier law

$$\mathbf{q} = -k\nabla\theta \tag{8}$$

where k is the thermal conductivity, taken to be 42.7 J s^{-1} m^{-1} K^{-1}. Plastic working generates heat per unit volume at the rate

$$\Gamma^{\mathrm{pl}} = \eta\sigma : \dot{\epsilon}^{\mathrm{pl}} \tag{9}$$

where Γ^{pl} is the rate of heat generation due to plastic working, $\dot{\epsilon}^{\mathrm{pl}}$ is the plastic strain rate and η is the heat conversion factor, taken to be 0.9. The temperature field θ is spatially discretized as

$$\theta = N^N(x)\theta^N \tag{10}$$

where θ^N are the nodal temperatures. Combining the thermal energy balance with the mechanical energy balance, and discretizing the fields, one finds that the variational statement of the energy balance obtained by the standard Galerkin approach leads to

$$\begin{bmatrix} K_{uu} & K_{u\theta} \\ K_{\theta u} & K_{\theta\theta} \end{bmatrix} \begin{bmatrix} \Delta u \\ \Delta\theta \end{bmatrix} = \begin{bmatrix} F_u \\ F_\theta \end{bmatrix} \tag{11}$$

where Δu, $\Delta\theta$ are the incremental displacement and temperature; K_{ij} are the submatrices of the fully coupled Jacobian matrix; F_u and F_θ are the mechanical and thermal residual vectors, respectively. The equations are fully coupled and must be solved simultaneously. The lateral boundary conditions are the periodicity conditions

$$u_i|_{x=0} = u_i|_{x=L} \qquad i = 1, 2 \tag{12}$$

where $u_i, i = 1, 2$ are the displacements in the X and Y directions. The boundary conditions on the traction-free surfaces are:

$$\begin{aligned} \sigma_{22} &= 0 \\ \sigma_{12} &= 0 \end{aligned} \tag{13}$$

for

$$\begin{aligned} &y = 0, \quad 0 \leqslant x \leqslant L \\ &y = H_1 + H_2, \quad 0 \leqslant x \leqslant L \\ &y = H_1, \quad 0 \leqslant x \leqslant L_1 \\ &y = H_1, \quad L - L_2 \leqslant x \leqslant L \end{aligned} \tag{14}$$

The initial conditions are those corresponding to an incident shear wave:

$$\begin{aligned} v_1 &= \frac{V_0}{2}\sin\theta \\ \sigma_{12} &= \frac{1}{2}\rho c_2 V_0 \sin\theta \end{aligned} \tag{15}$$

for $0 \leqslant x \leqslant L$, $0 \leqslant y \leqslant c_2\Delta t$, and

$$v_1 = 0 \tag{16}$$

everywhere else. Here V_0 is the projectile velocity and θ is the skew angle. Initially, all other components of stress and particle velocity are zero.

Results of simulations with a mesh size of 5 μm are shown in Figs. 31–34. Contour plots of stress σ_{12} and the temperature θ at 0.74 μs are shown in Figs. 31 and 32. Contour plots for the strain ϵ_{12} (see Zhang, 2005) are similar to those for temperature. The region of elevated stress σ_{12} extends much farther in front of the crack tip than the regions of elevated temperature and strain ϵ_{12}. Figs. 33 and 34 show the nodal temperature along the crack plane and perpendicular to it. All temperatures are in degrees Kelvin. Each node is identified by a triangular symbol. Along the crack plane the temperature rises sharply near the crack tip. The temperature affected zone extends farther in front of the crack tip than behind it because, for a stationary crack, the plastic deformation is primarily in front of the crack tip. Perpendicular to the crack plane, the temperature is distributed almost symmetrically with respect to the crack plane. The temperature rises to a maximum of

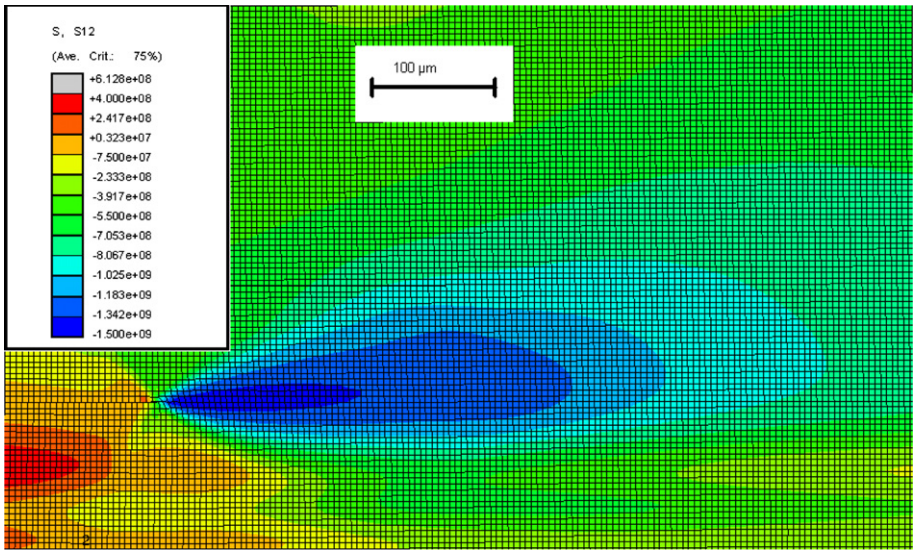

Fig. 31. Contour plot of the stress σ_{12} at 0.74 μs (mesh size 5 μm).

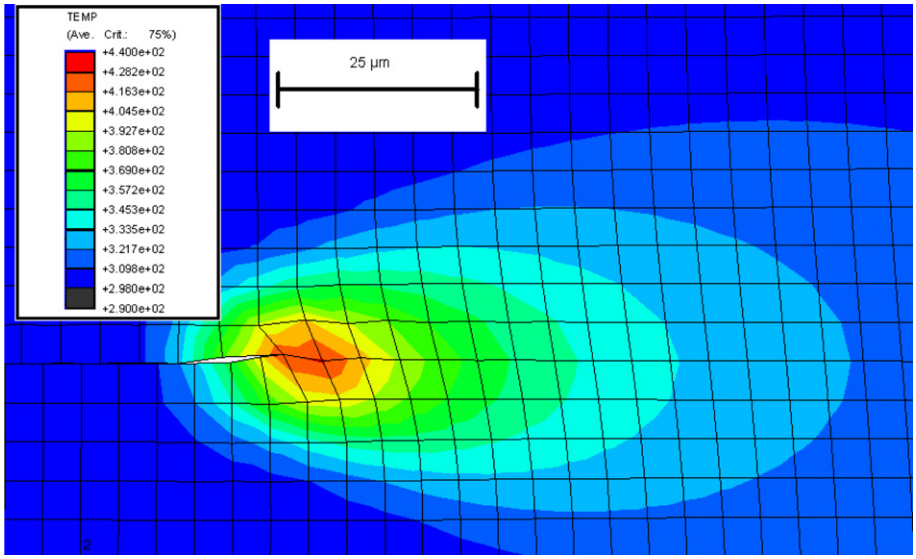

Fig. 32. Contour plot of the temperature distribution at 0.74 μs (mesh size 5 μm).

172 °C at the tip of the crack, but to only 30 °C at 10 μm above or below the crack plane. Overall, the temperature rise is less than was expected from the intense shear observed in the recovered plates.

In order to investigate the effects of mesh size, three different mesh sizes were used: 1.25 μm, 2.5 μm and 5 μm. The total duration of the simulation is set to be one fourth of the pulse duration because that is the maximum time for which the simulation could be completed using the smallest mesh. A quadratic fit is used to extrapolate values to those for a hypothetical mesh of zero size. The results are summarized in Fig. 35. Temperatures tend to increase with decreasing mesh size in regions ahead of the crack tip as expected for calculations that provide better descriptions of the intense deformation in this region. Quadratic extrapolation is used to estimate the temperatures at a mesh size of zero. Although quadratic extrapolation is used, the extrapolated values do not differ much from those that would be obtained by using linear extrapolation of results for the two smallest mesh sizes. From a theoretical perspective, the latter extrapolation is more appropriate as the

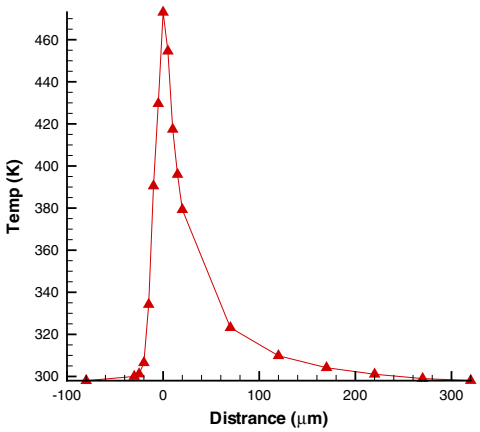

Fig. 33. Temperature distribution along the crack plane at 0.74 μs (mesh size 5 μm).

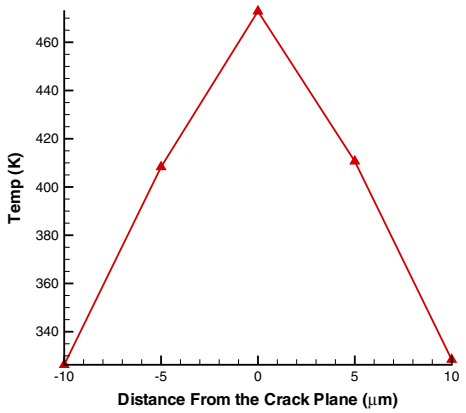

Fig. 34. Temperature distribution perpendicular to the crack plane at the crack tip at 0.74 μs (mesh size 5 μm).

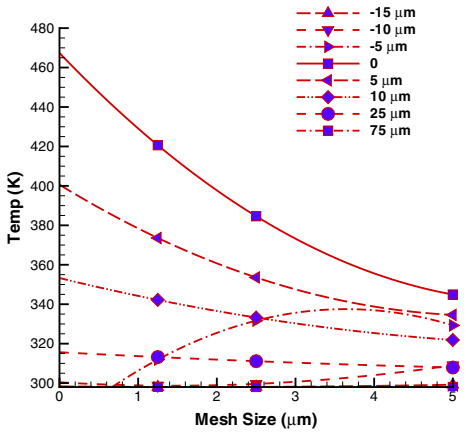

Fig. 35. The mesh size effect for temperature distribution along the crack plane at 0.185 μs.

numerical method used is a first-order accurate method. It appears that at time $t = \frac{1}{4}\Delta t$ the temperature for a mesh size of zero will increase by a maximum of approximately 170 °C at the tip of the crack. Temperature at the crack tip increases essentially linear with time so that a maximum temperature rise for a mesh size of zero is

projected to be approximately 680 °C. The temperature distributions perpendicular to the crack plane for different mesh sizes are shown in Fig. 36. As the mesh size decreases, the width of the band decreases. The amplitude of the temperature rise, and its extent along the crack plane, are smaller than suggested by the observed shear bands.

In order to examine the effects of changes in the power-law parameters that can be expected to enhance shear strain localization, we considered changes that reduce the strain hardening (even allowing strain softening), reduce strain-rate hardening, and increase thermal softening. It is found that these variations in the parameters of the power-law plasticity model have little effect on the resulting temperature field. Details can be found in Zhang (2005).

Shear band formation is complicated and can involve failure of the material in the developing band. Through introducing a simple shear failure model in the current thermal-plastic scheme, it is possible to investigate the effects of material failure on shear band formation. We assume that the damage to the material through plastic deformation can be characterized by a damage parameter ω,

$$\omega = \frac{\bar{\epsilon}_0^{\mathrm{pl}} + \sum \Delta\bar{\epsilon}^{\mathrm{pl}}}{\epsilon_{\mathrm{f}}^{\mathrm{pl}}} \tag{17}$$

where $\bar{\epsilon}_0^{\mathrm{pl}}$ is the initial value of the equivalent plastic strain, $\Delta\bar{\epsilon}^{\mathrm{pl}}$ is the equivalent strain increment at each time increment, and $\epsilon_{\mathrm{f}}^{\mathrm{pl}}$ is the preset failure strain. The initial value $\bar{\epsilon}_0^{\mathrm{pl}}$ is taken to be zero although a small amount of plastic deformation may be caused by the incident longitudinal wave for the experiments at the higher impact velocities. When the damage parameter reaches 1, (i.e., when the accumulated plastic strain is equal to the preset failure strain), the material is assumed to fail. For the FEM scheme, the possibility of failure is examined at the material integration points for each element. If all the integration points inside an element fail, this element fails. In our calculations, the linear, reduced-integration, square elements contain only one integration point for each element. Thus, if the failure condition is met, that material element fails. Again calculations were done on a 5 μm mesh. Contour plots of stress σ_{12} and temperature θ at 0.74 μs are shown in Figs. 37 and 38 for a failure strain of 10%. Each element is initially a 5 μm square. Figs. 39 and 40 show the temperature distributions along the crack plane and perpendicular to the crack plane at $t = 0.739$ μs for failure strains of 10%, 20%, and 40%. The origin of the coordinate system shown is at the initial position of the crack tip. At the smaller failure strains, a band-like structure is clearly formed along the crack plane. It remains roughly on the crack plane with small wavy features associated with deformation of the mesh in front of the crack tip. The smaller the failure strain, the longer the band. However, the maximum temperature at $t = 0.739$ μs is lower for the smaller failure strain. For the model without failure the maximum temperature is 474 K. If the failure strain is set to be 10%, the maximum temperature is 357 K; if the failure strain is 20%, the max temperature is 408 K; if the failure strain is 40%, the temperature distribution is the same as that of the model that does not account for failure. The last observation is expected because the maximum equivalent shear strain for the

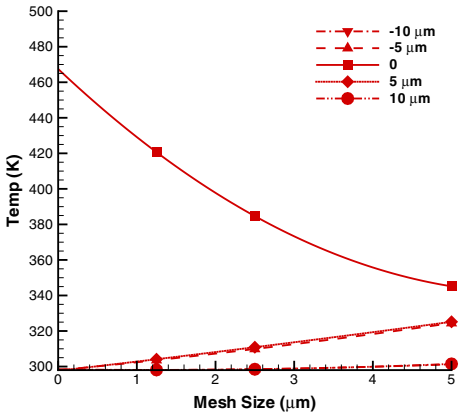

Fig. 36. The mesh size effect for temperature distribution perpendicular to the crack plane at 0.185 μs.

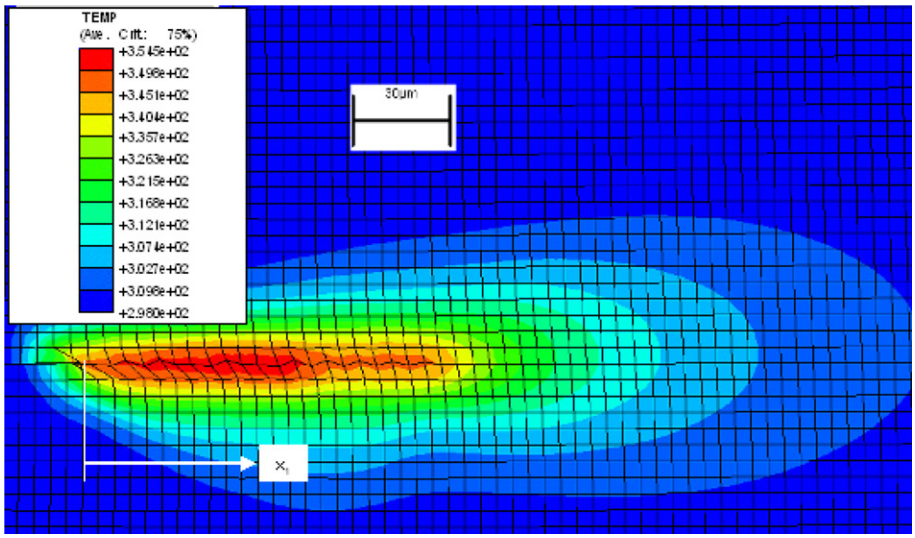

Fig. 37. Contour plot of temperature at 0.74 μs for $\epsilon_f^{pl} = 0.1$.

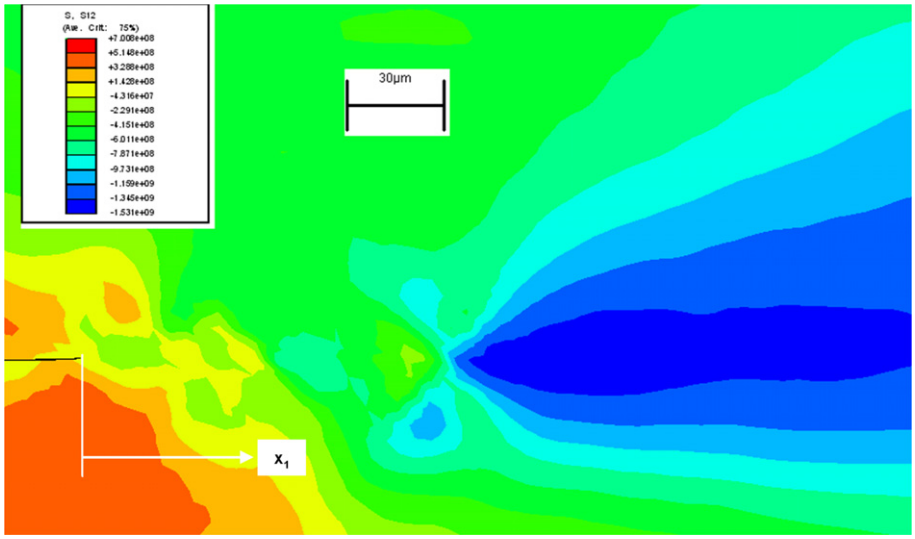

Fig. 38. Contour plot of shear stress σ_{12} at 0.74 μs for $\epsilon_f^{pl} = 0.1$.

simulations without failure is approximately 36%. The observed effects are understandable since when the shear stresses in a failed element are set to zero, additional stress is transferred to an adjacent element.

If the temperature marking the length of the band is taken to be one-half of the maximum temperature reached for failure at a strain of 10%, i.e., 327.5 K, then the length of the band is 150 μm, 100 μm and 80 μm for the models with shear failure at strains of 10%, 20%, and 40%, respectively. As for the temperature distribution perpendicular to the crack plane, the maximum temperature drops as the failure strain is reduced. The maximum temperature is achieved at the crack plane and its values are 352 K, 408 K and 474 K for the models with shear failure at strains at 10%, 20%,and 40%, respectively. The temperature is essentially symmetrical with respect to the crack plane. Overall, smaller strains at failure generate longer bands with lower peak temperatures. Far ahead of the crack tip, but still inside the band region, the temperature is higher for failure at smaller strains. It is also found (see Zhang, 2005) that the smaller the flow stress, the longer the band and the lower the plateau temperature. Again, the temperature increases and the shear band lengths are less than

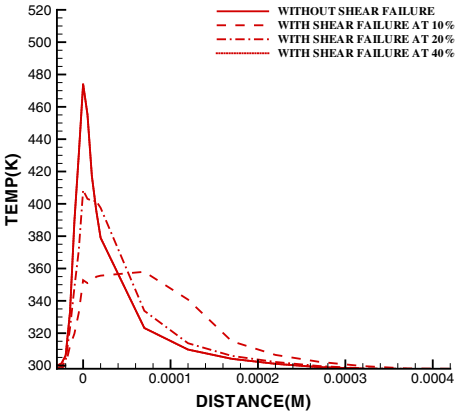

Fig. 39. Temperature distribution along the crack plane at 0.74 μs for different failure strains.

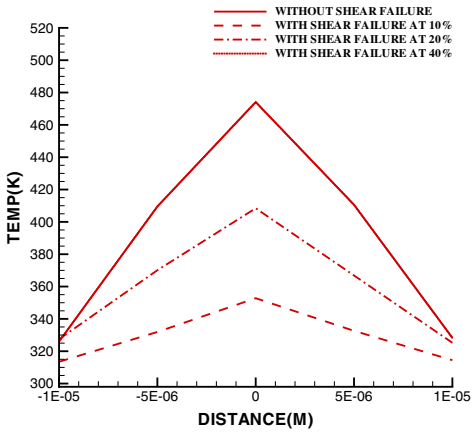

Fig. 40. Temperature distribution perpendicular to the crack plane at 0.74 μs for different failure strains.

expected from the observations of the recovered samples. From the previous discussion of mesh size effects, the computed temperature increases and shear band lengths would be increased if smaller mesh sizes were used.

6. Discussion of results

Pressure–shear plate impact experiments on pre-cracked steel plates subjected to Mode II loading have led to reproducible velocity–time profiles that are essentially describable by calculations based on elastic wave theory. For higher speed impacts (i.e., 125 m/s), the tops of the wave fronts show rounding indicative of the impacts causing some modest plastic deformation. For a lower speed (91 m/s) impact there is no rounding of the incident wave pulse. Thus, the loading in the experiments corresponds essentially to the idealized elastodynamics problem of a semi-infinite plane crack subjected to an incident Mode II plane wave at normal incidence. The measured velocity–time profiles at a point on the rear surface of the plate appear to be reliable, especially after the TDI was modified to improve the measurement of the transverse displacement. The FEM simulations of the impact problem appear to provide reasonably satisfactory explanations of the measured velocity–time profiles – even when the steel is taken to be elastic as it is in Section 2. One disappointing aspect of the simulations is the relatively large dispersion that is observed in the calculated shear pulses. Because of this dispersion, the calculated transverse velocity–time profiles lack the sharpness of the pulses observed in the experiments.

The principal challenge that arises in the interpretation of these experiments is in understanding the generation of the long shear bands that are observed. Attempts to simulate the formation of these bands has been only partially successful even though considerable effort has been put into using realistic thermo-viscoplastic models for the shearing resistance of the 4340 VAR steel and a supercomputer has been used to make it possible to have mesh sizes that are significantly smaller than the width of the shear band. Further refinement of the mesh size could lead to improved agreement through resulting in higher calculated temperatures and longer bands. However, the discrepancy between the lengths of the short bands obtained in the simulations and the long bands observed in the experiments is so great that it does not appear that mesh refinement alone would suffice to reconcile theory and experiment. From the attempts reported here to modify the power law model for the shearing resistance to make the shearing response less stable, it does not appear likely that realistic changes in the parameter values of the model are likely to increase band lengths enough for them to agree with measured lengths. Also, artifacts of the experiment, such as the effects of multiply reflected waves, do not appear to be responsible for a major increase in the lengths of the bands that are observed.

Of all the factors examined here, the one that shows most promise for explaining the length of the observed bands appears to be the inclusion of a critical shear strain at which the shearing resistance is lost completely. That such a loss in strength would lead to substantially longer bands is evident from the elastodynamic solution for a propagating shear band in the Mode III case, Zhang and Clifton (2003), in which the speed of propagation of the band c_b is given by

$$c_b = \left(\frac{\tau^*}{\tau^p}\right)^2 c_2 \tag{18}$$

where τ^* is the shear stress in the incident elastic wave, τ^p, is the (constant) shearing resistance of the band, and c_2 is the elastic shear wave speed. When the shearing resistance is allowed to fall to zero behind the front of the shear band the equation corresponding to Eq. (18) is (Zhang, 2005)

$$c_b - c_f = \left(\frac{\tau^*}{\tau^p}\right)^2 c_2 \tag{19}$$

where c_f is the speed of propagation of the front of the failed region within the band. Comparison of Eqs. 18 and 19 shows that the front of the shear band is predicted to propagate much faster if the front of the band is followed by a failed region that propagates at a speed c_f, comparable to the speed c_b.

While it is clear from Eqs. 18 and 19 that reduced shearing resistance increases the length of the shear band, the mechanism responsible for this reduction is less clear. The usual explanation is that heating due to a high rate of plastic working causes an increase in temperature that decreases the shearing resistance causing further increase in the local rate of plastic straining. This process leads to a thermoplastic instability in which pronounced loss in shearing resistance occurs. Measurements of greatly elevated temperatures, especially in the 2D high speed infrared camera data reported in Guduru et al. (2001), provide strong support for attributing the loss in shearing resistance to a thermoplastic instability. Furthermore, the introduction of a fluid model with a viscosity that decreases exponentially with increasing temperature (Zhou et al., 1996b and Li et al., 2001) provides the strong loss in shearing resistance that appears to be necessary to describe results of previous Kalthoff-like experiments: Zhou et al. (1996a) and Guduru et al. (2001). One concern about this model is that the temperature elevation at the time the rate dependent critical strain is reached (see, e.g., Li et al., 2001) is rather small to support an explanation based on sufficiently high temperatures being generated by plastic heating. In our case, their model would involve switching over to a viscous fluid collapse model at strains of the order of 0.04 – at which our simulations indicate that the temperatures are too low for the steel to be regarded as fluid-like. Furthermore, the shear weakening of the fluid with increasing temperature would tend to moderate the rate of increase in temperature, making it more difficult to obtain the high temperatures reported for the experiments, Guduru et al. (2001).

Measurements of the dynamic shearing resistance of a 4340 VAR steel, with almost the same heat treatment as that used for the experiments reported here, have been made in a modified double shear experiment Klepaczko and Klosak (1999) in which a disk is sheared in a notched annulus of a circular plate that is supported by an outer shoulder and loaded by a cylindrical bar on the central region of the disk. This sample is loaded at

impact velocities ranging from 20 m/s to 130 m/s. As the impact velocity increases the energy absorbed and the strain to failure decrease dramatically at an impact velocity of approximately 100 m/s. The authors attribute the failure to reaching a critical impact velocity at which the adiabatic stress–strain curve, in shear, exhibits a horizontal tangent at a critical shear strain. Their simulations show that this critical shear strain decreases dramatically at impact velocities above the critical impact velocity of approximately 100 m/s. These results may have bearing on the results of the pressure–shear impact experiments reported here since the energy densities at which they (Klepaczko and Klosak, 1999) find the dramatic loss in shearing resistance are substantially lower than those calculated for the shear bands that are obtained in our simulations.

To obtain better understanding of the failure mechanism that leads to the long bands it appears to be essential to make more detailed microscopic examinations of the recovered samples. The brittleness of the material in the bands has hampered attempts to make TEM samples to obtain the microstructure of the material within the band. Making such observations is a goal for further investigations.

Acknowledgements

This research was supported primarily by the Army Research Office (ARO). In its later stages it was supported by the NSF-sponsored Materials Research Science and Engineering Center at Brown University on "Micro- and Nano-Mechanics of Electronic and Structural Materials". The authors are grateful for the support of both ARO and NSF. The support from The National Center for Supercomputing Applications at University of Illinois at Urbana-Champaign for providing computational resources is also greatly appreciated.

References

Clifton, R.J., Klopp, R., 1985. ASM Metals Handbook, 9th ed., vol. 8. ASM International, Materials Park, OH, Ch. Mechanical Testing, pp. 25–38.

Field, J.E., Walley, S.M., Bourne, N.K., Huntley, J.M., 1994. Experimental methods at high rates of strain. Journal de Physique IV Colloque C8, 3–22.

Follansbee, P.S., 1985. ASM Metals Handbook, 9th ed., vol. 8. ASM International, Materials Park, OH, Ch. Mechanical Testing, pp. 198–203.

Guduru, P.R., Ravichandran, G., Rosakis, A.J., 2001. Observation of transient high temperature vortical microstructures in solids during adiabatic shear banding. Physical Review E 64, 036128-1–036128-6.

Hartley, K.A., Duffy, J., Hawley, R.H., 1985. ASM Metals Handbook, 9th ed., vol. 8. ASM International, Materials Park, OH, Ch. Mechanical Testing, pp. 218–228.

Kalthoff, J.F., 1987. Shadow optical analysis of dynamic shear fracture. Progress in Material Sciences 814, 531–538.

Kalthoff, J.F., 2000. Modes of dynamic shear failure in solids. International Journal of Fracture 101, 1–31.

Kim, K.S., Clifton, R.J., Kumar, P., 1977. A combined normal and transverse displacement interferometer with an application to impact of y-cut quartz. Journal of Applied Physics 48, 4132–4139.

Klepaczko, J.R., Klosak, M., 1999. Numerical study of the critical impact velocity in shear. European Journal of Mechanics A/Solids 18, 93–113.

Lambros, J., Rosakis, A.J., 1994. Dynamic decohesion of bimaterials: experimental observation and failure criteria. In: Okabayashi, H., Shingubara, S., Ho, P. (Eds.), NSF/ONR Symp. Dynamic Failure of Modern Materials, vol. 1 of NSF/ONR Symp. NSF/ONR, American Institute of Physics, New York, pp. 25–38.

Li, S., Liu, W., Qian, D., Guduru, P.R., Rosakis, A.J., 2001. Dynamic shear band propagation and micro-structure of adiabatic shear band. Computer Methods in Applied Mechanics and Engineering 191, 73–92.

Liu, C., Huang, Y., Rosakis, A.J., 1995. Shear dominated transonic interfacial crack growth in a bimaterial-II. Asymptotic fields and favorable velocity regimes. Journal of the Mechanics and Physics of Solids 43, 189–206.

Mason, J.J., Rosakis, A.J., Ravichandran, G., 1994. Full field measurements of the dynamic deformation field around a growing adiabatic shear band at the tip of a dynamically loaded crack notch. Journal of the Mechanics and Physics of Solids 42, 1679–1697.

Mgbokwere, C.O., May 1996. Experimental study and micromechanical modelling of shear banding in an AISI 4340 VAR steel. Ph.D. thesis, Brown University, Providence, RI.

Ramesh, K.T., Narasimhan, S., 1996. Finite deformations and the dynamic measurement of radial strains in compression Kolsky bar experiments. International Journal of Solids and Structures 33, 3723–3738.

Ravichandran, G., Clifton, R., 1989. Dynamic fracture under plane wave loading. International Journal of Fracture 40, 189–200.

Rogers, H.C., 1979. Adiabatic plastic deformation. Annual Review of Materials Science 9, 283–311.

Tanimura, S., Duffy, J., 1986. Strain-rate effects and temperature-history effects for three different tempers of 4340 VAR steels. International Journal of Plasticity 2, 21–35.

Zhang, Z., Aug 2005. Shear band propagation from a crack tip subjected to shear wave loading. Ph.D. thesis, Brown University, Providence, RI.

Zhang, Z., Clifton, R.J., 2003. Shear band propagation from a crack tip. Journal of the Mechanics and Physics of Solids 51, 1903–1922.

Zhou, M., Ravichandran, G., Rosakis, A.J., 1996a. Dynamically propagating shear bands in impact-loaded prenotched plates – i. investigation of temperature signatures and propagation speed. Journal of the Mechanics and Physics of Solids 44, 981–1006.

Zhou, M., Ravichandran, G., Rosakis, A.J., 1996b. Dynamically propagating shear bands in impact-loaded prenotched plates – ii. numerical simulations. Journal of the Mechanics and Physics of Solids 44, 1007–1032.